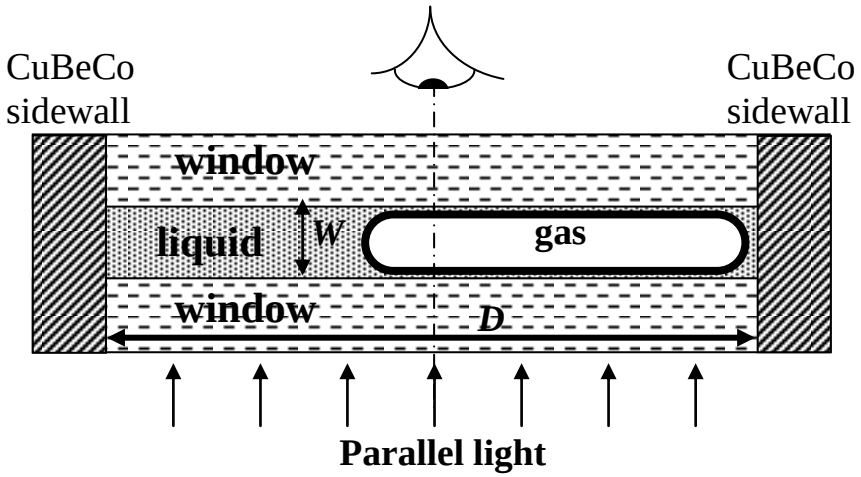

Figure 1. A cross-section view of the cylindrical sample cell. The fluid volume is contained between two sapphire windows and a CuBeCo alloy ring (sidewall). The dimensions (*W*, *D*) of the cell are indicated. The semi-circular liquid-gas meniscus between the two parallel windows is shown. This interface appears dark in the images because the liquid-gas meniscus refracts the normally incident parallel light away from the cell axis.

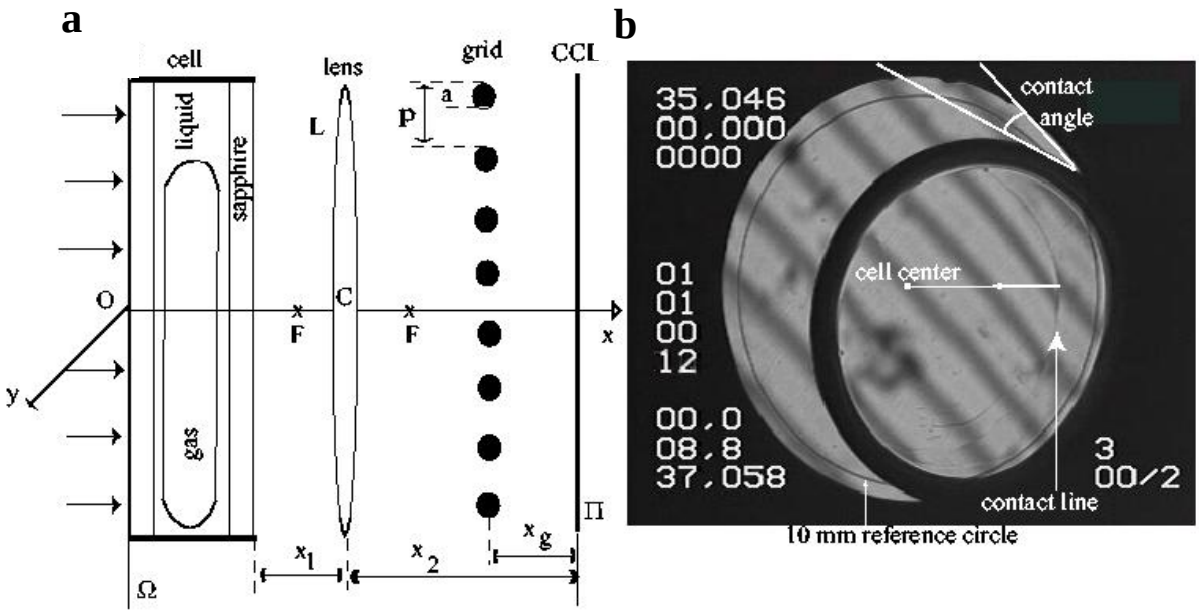

Figure 2. (a) The cell (from experiment B) is a *D=12 mm* diameter cylinder made of CuBeCo containing a *W=1.664 mm* layer of SF_6 sandwiched between two sapphire windows (*9 mm* thick). The convergent lens *L*, with focal point *F* and the center *C*, projects the out-of-focus grid image on the CCD plane *Π* (panel b). This system can detect a density change of up to $7.8 \times 10^{-5} g/cm^3$/pixel. The density may then be found by integrating the local density changes from a given reference density. This technique is sufficient to detect steep density gradients in the fluid. It is only capable, however, of detecting 4.3% constant density gradient change across 1 cm length of the cell of SF_6. In a liquid-gas mixture, these displacements may be analyzed using the paraxial approximation of geometrical optics. (b) Shown is the defocused grid image recorded by the CCD camera. The evaporation of the liquid film between the sapphire window(s) and the gas bubble leads to a gas-liquid-solid contact line. The part of the grid shadows that is not distorted is to the right of the contact line indicating the existence of a dry gas-solid interface. When heating is first applied, a receding contact line and a simultaneous change in the bubble/sidewall contact angle, shown above, are seen. The heat transfer through the cell's copper sidewall evaporates the liquid film causing this change in the bubble/sidewall contact angle. Also shown is the 10 mm diameter reference circle, the center of the cell, the reference line, and the point used in Figure 9 and Figure 10.

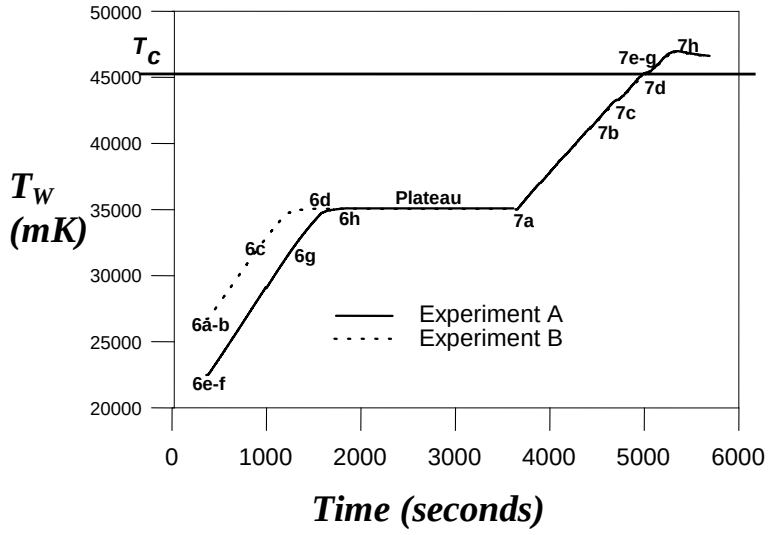

Figure 3. Temperature ramp applied to cells A and B. The initial ramp has an 8.7 mK/s rate followed by a 40 minutes plateau and a 7.4 mK/s ramp. T_W is the temperature measured in the copper sidewall. Also shown are the times and temperatures for the sequence of images in Figures 6 and 7.

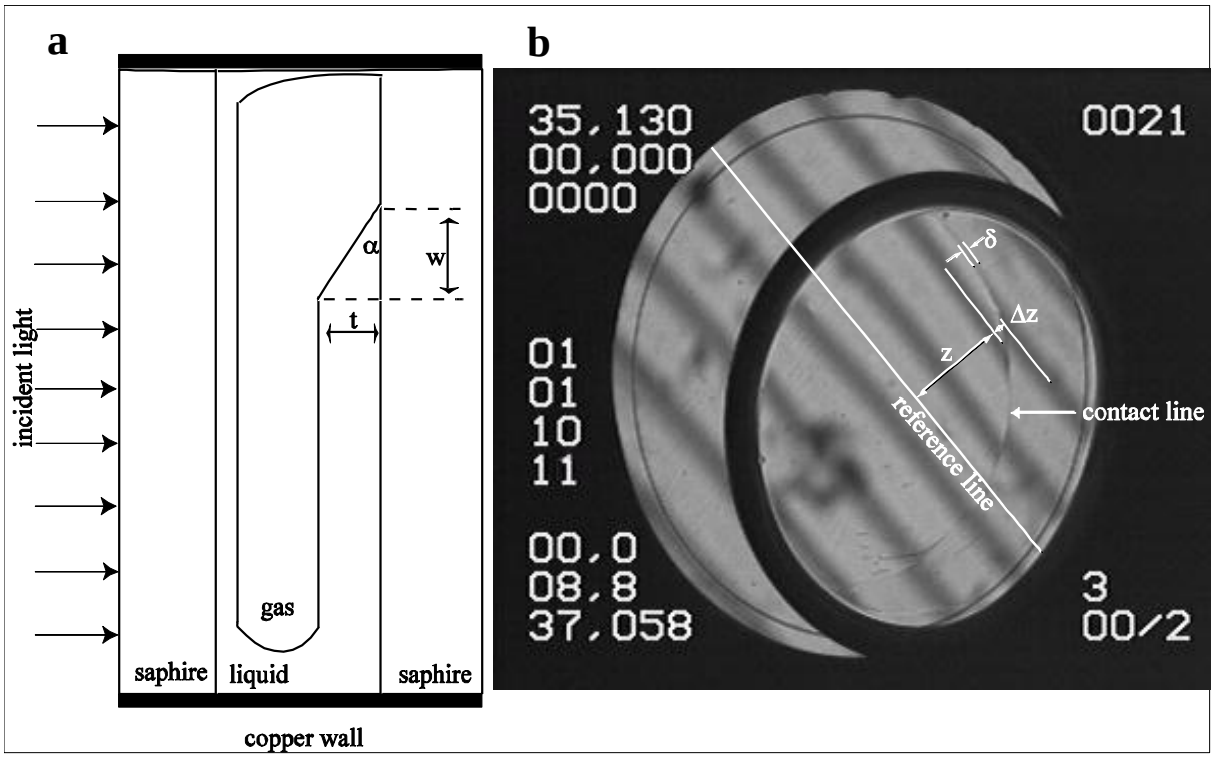

Figure 4. (a) The tilted gas-liquid interface due to liquid evaporation leads to a contact line. (b) The tilt angle induces a significant displacement of the grid shadows. The shadow displacement depends on the tilt angle α, the width w, and the thickness t of the film (see text for details). Also shown are z, Δz, δ, and the reference line used in the calculations of the thickness t of the film.

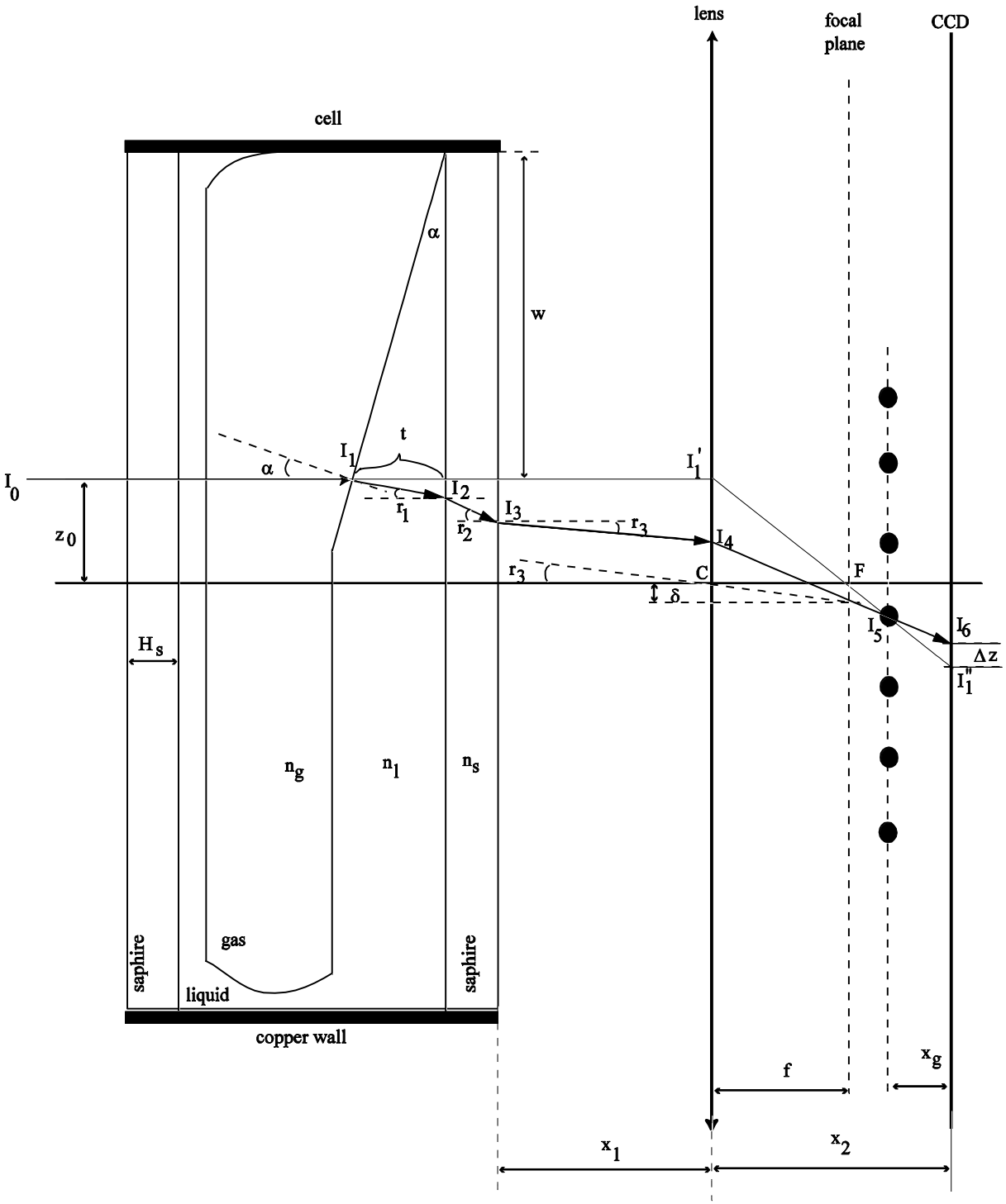

Figure 5. Ray tracing through the cell and the optical system. The tilt angle of the gas-liquid interface is exaggerated for illustration purposes and is shown only on one side for simplicity. An incident ray I_0, passing at distance z_0 from the optical axes, would remain parallel to the optical axes if the interface is not tilted with respect to the sapphire windows and would hit the CCD plane at I_1". If there is a tilt angle α of the gas-liquid interface, then the ray starting at I_0 would hit the CCD plane at I_6 following successive refractions at I_1, I_2, I_3, and I_4. The displacement of the shadow Δz depends on the tilt angle α of the interface and its thickness t.

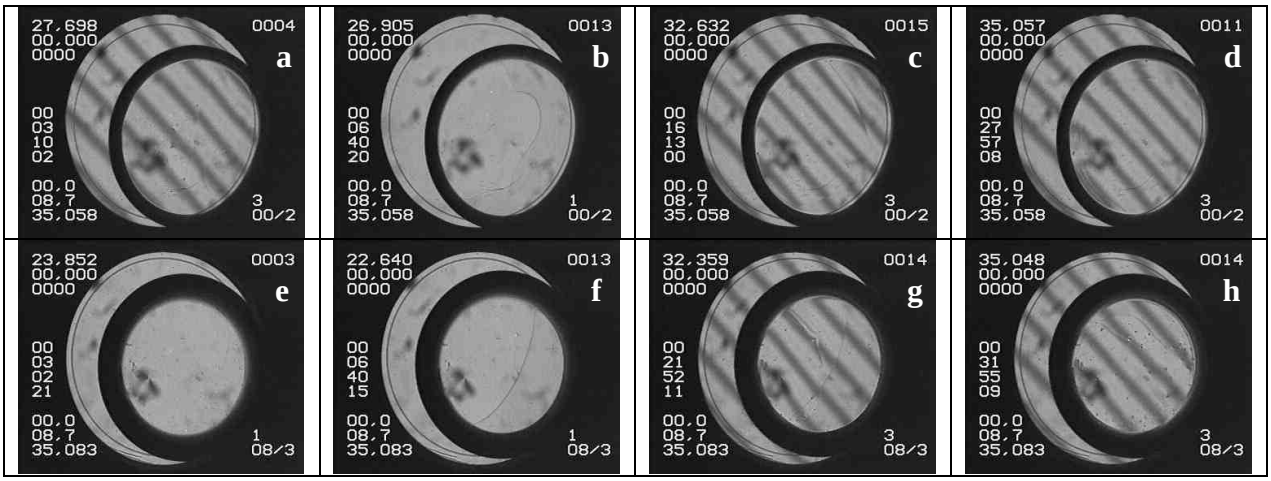

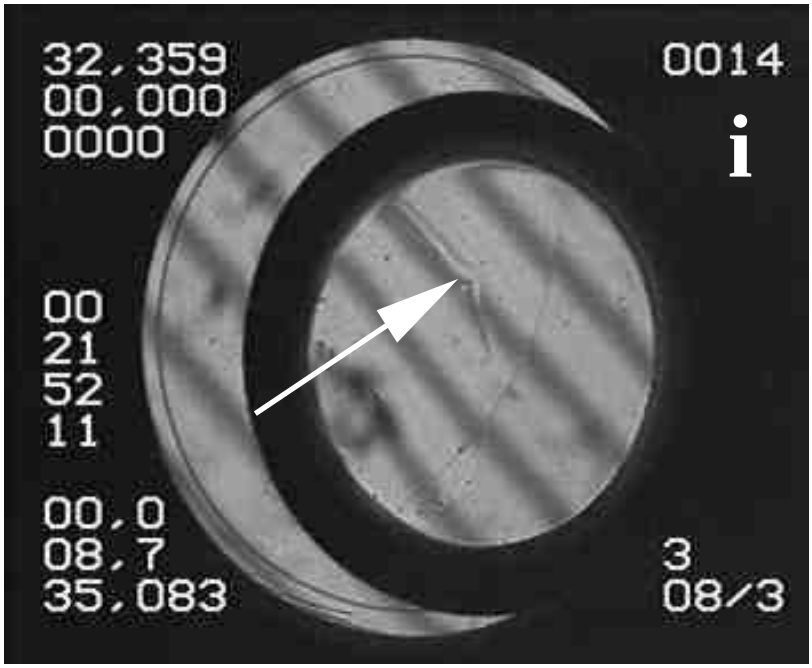

Figure 6. Shown is a sequence of images from the initial ramp of experiments B (a-d) and A (e-h). In these experiments the compressed bubble touches the sidewall. The initial state of the gas bubble for these two experiments is shown in Figure 6a (experiment B with heating started) and 6e (experiment A before heating). The cell used in experiment A is thicker than the cell in experiment B (see Table 1). The liquid-gas meniscus produced a wider dark region in the image (e-h). The film contact lines appear when the heating begins and Figure 6f shows it 20 seconds after heating started. Figures 6b-c and 6f-g show the contact line with and without the grid present. Figure 6i is an enlargement of 6g and it shows that one of the two contact lines (there is one on each wall) is distorted by a particle deposited on the sapphire windows as indicated by the arrow.

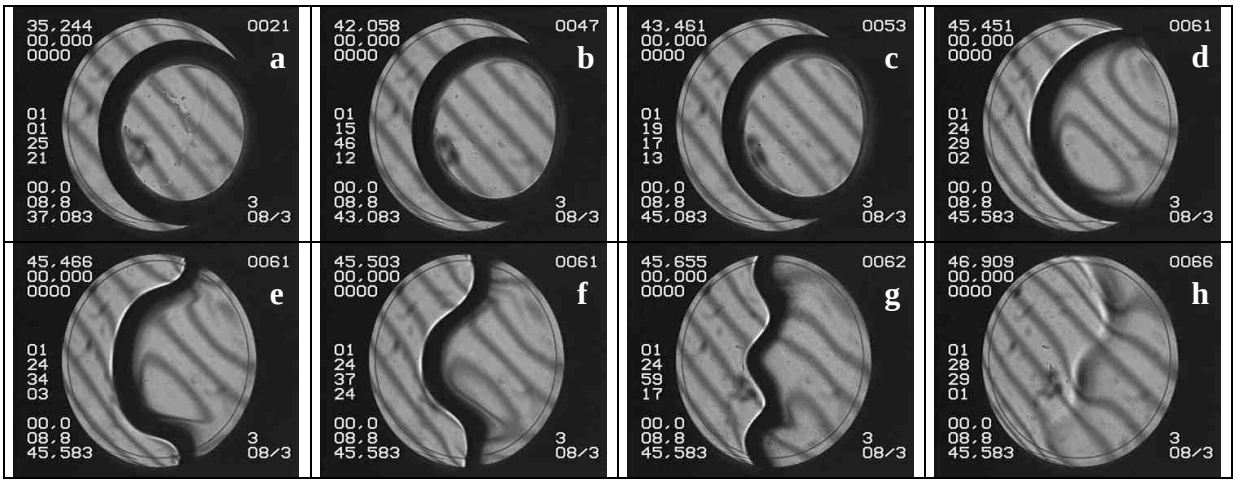

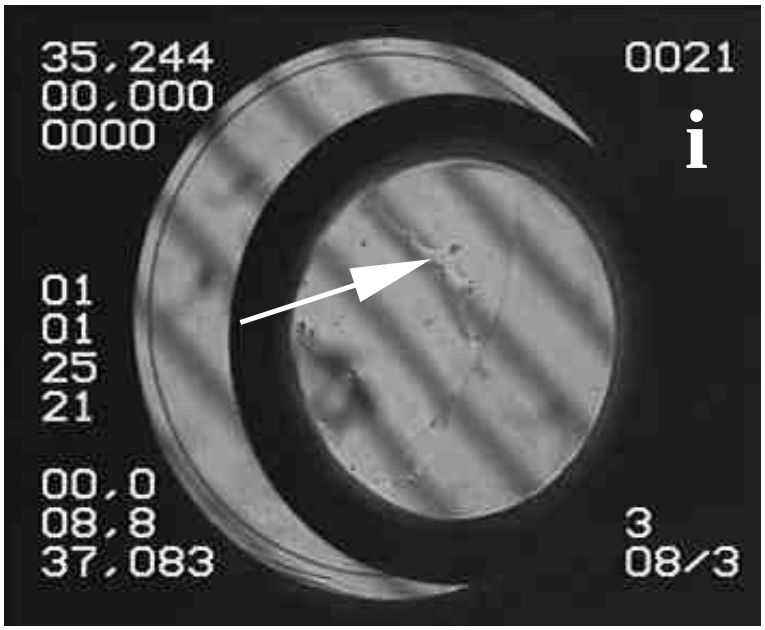

Figure 7. The ramp shown in Figure 3 is also performed in experiment A. The fast spreading of this bubble appears to be more energetic than the thin bubble in experiment B. Figure 7i is an enlargement of 7a and it shows that one of the two contact lines (there is one on each wall) is distorted by some particles deposited on the sapphire windows as indicated by the arrow. This shows that these thin lines are contact lines in that they can be pinned by a defect while advancing or receding.

Figure 8. Shown are some of the events that occurred in the final portion of a ramp similar to the ramps shown in Figure 3 in a cell filled with CO_2. This cell contains 3 thermistors and a piston to vary the fluid density between ramps. In this case the fluid was at $\delta\rho$= -3.5% below the critical density. Figure 8a shows that a cluster of bubbles has formed at the edge of the cell far below T_C. One of these bubbles has coalesced with the large bubble producing a hot plume that travels toward the center of the large bubble. Figure 8b, at approximately T_C, shows a

considerably distorted grid shadow image with critical opalescence at the sidewall in the region just where the bubbles were nucleating. The dynamical activity suddenly stops at about the same time as this layer forms. The particular phase distribution that existed just before the critical temperature was passed appears to be frozen in place. The image in Figure 8c is above the critical temperature T_C and the grid shadows in this image shows significant density changes. Slower mass fluxes continue, however, and the system evolves to a uniform super-critical fluid not long after Figure 8c.

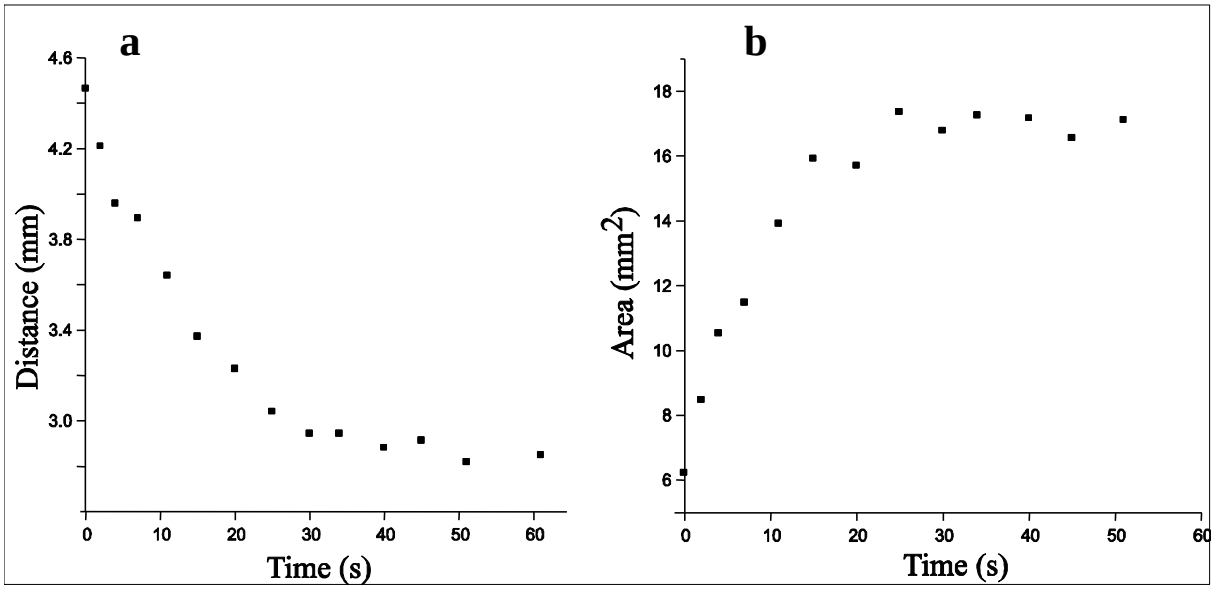

Figure 9. (a) The position of the contact line with respect to the center of the cell versus time (see Figure 2) after heating begins. (b) The dry area behind the triple contact line and the interior of the dark meniscus region rapidly increases while the contact line moves toward the cell's center.

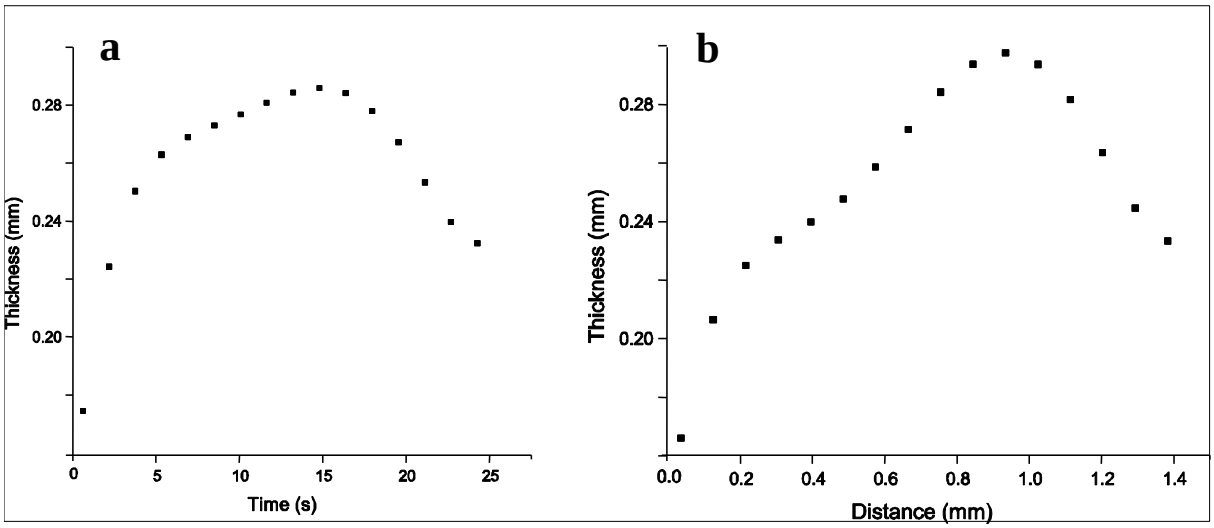

Figure 10 The thickness of the wetting film near the triple contact line was computed using the wedge model at the position shown by the point in Figure 2b (data from experiment B). (a) Estimated thickness of the wetting film versus time calculated at the beginning of the second heating ramp with respect to cell's center. (b) Estimated spatial profile of the contact line based on the relationship between the distance swept by the contact line and the elapsed time.

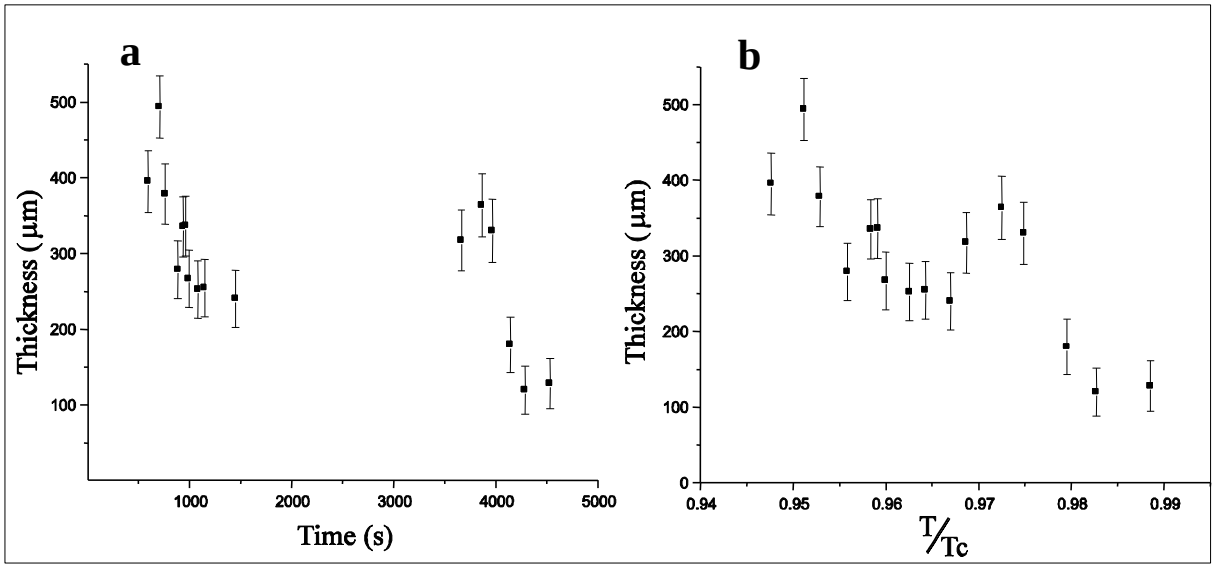

Figure11. Estimated thickness of the wetting film versus time (a) and versus relative temperature (b). The data refer to experiment B and used the linear wedge model. The error bars reflect the uncertainty in the measurements of the contact line width.

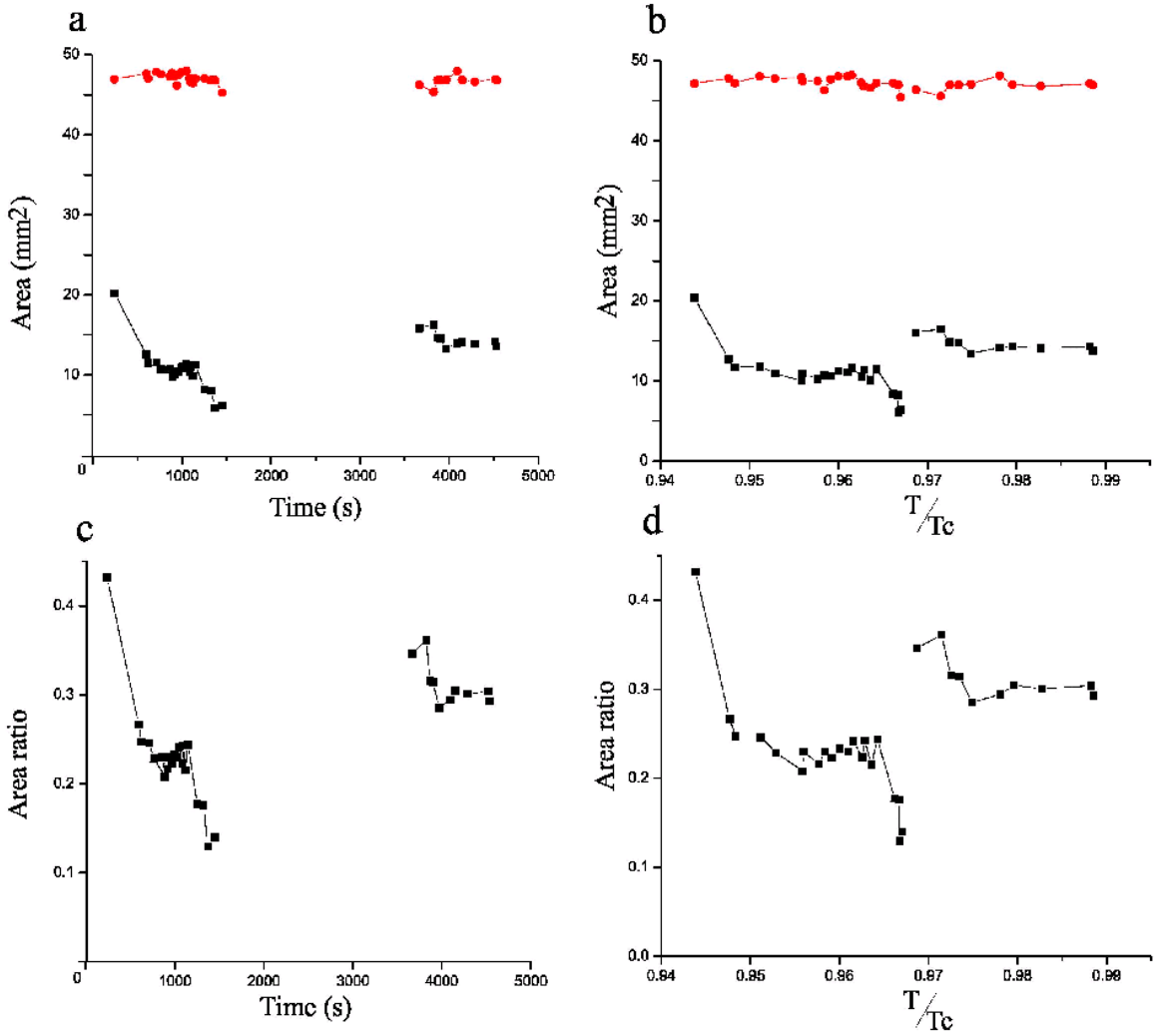

Figure 12. Dry area (squares on panels a and b) and the total area of the gas bubble (circles on panels a and b) versus time (panel a) and relative temperature (panel b). The data are from experiment B and both areas were measured with respect to the interior of the dark meniscus. The total area of the gas bubble is constant during heating (circles on panels a and b). The ratio of the dry area, behind the contact line, to the total area of the gas bubble, versus time (panel c), and versus the relative temperature (panel d) is shown.